AN ABSTRACT OF THE THESIS OF

Wei-Che Hsu for the degree of Master of Science in Electrical and Computer Engineering presented on June 8, 2020.

Title: Silicon Microring Resonator Driven by High-Mobility Conductive Oxide Capacitor

Abstract approved:

____

Alan X. Wang

Silicon photonics has rapidly become one of the most promising photonic integration platforms. Especially, microring resonator (MRR) plays a pivotal role in silicon photonics and has been widely used for electro-optic (E-O) modulators and wavelength filters due to its small footprint, low energy consumption, and high quality factor (Q-factor). Recently, indium-tin-oxide (ITO) has emerged as a new material that can be integrated with silicon MRRs using a metal-oxide-semiconductor (MOS) structure, which can offer significantly enhanced E-O effect and better energy efficiency. However, the performance is limited by the relatively low electron mobility, which induces relatively high optical loss and degrades Q-factor. This thesis focuses on the demonstration of high Q-factor MRR driven by high mobility transparent conductive oxide (TCO) material. In the first part, a passive MRR is optimized by fabrication and theoretical design, which achieves a high Q-factor of 20,000. Next, a MRR with a titanium-doped indium oxide gate has been demonstrated to obtain a tunability of 42 pm/V with a high Q-factor above 3,600. Besides, a new method has been developed to

characterize the optical frequency free carrier mobility in the accumulation layer of the MOS structure. At the end of the thesis, different MRRs driven by high mobility TCO materials are compared. The simulation results indicate that an ultra-high tunability of 906 pm/V and a high Q-factor above 6,700 can be potentially achieved with slotted waveguide MRR.

©Copyright by Wei-Che Hsu
June 8, 2020
All Rights Reserved

Silicon Microring Resonator Driven by High-Mobility Conductive Oxide Capacitor

by
Wei-Che Hsu

A THESIS

submitted to

Oregon State University

in partial fulfillment of
the requirements for the
degree of

Master of Science

Presented June 8, 2020
Commencement June 2020

Master of Science thesis of Wei-Che Hsu presented on June 8, 2020

APPROVED:

Major Professor, representing Electrical and Computer Engineering

---

Head of the School of Electrical Engineering and Computer Science

---

Dean of the Graduate School

I understand that my thesis will become part of the permanent collection of Oregon State University libraries. My signature below authorizes release of my thesis to any reader upon request.

Wei-Che Hsu, Author

ACKNOWLEDGEMENTS

I would like to thank my advisor Dr. Alan Wang. When I first joined this group, I had no experience with this topic. I have learned not only theoretical knowledge but also the experience of fabrication from his guidance and teaching. I would also like to thank Dr. John F. Conley, Jr., Dr. Matthew Johnston, Dr. Pallavi Dhagat, and Dr. Burak Sencer for serving my committees. Thank you for your time.

I would like to thank MaSC Lab and EM Facility for their help in offering me the resources in my research. I really appreciate the support from Chris, Rick, Peter, and Teresa. When I got some questions in my research or problems with equipment, they always generously gave me the advice and taught me a lot. Thank you for all the help and for providing the equipment training.

All my labmates have also helped me a lot with my research, and they have helped me with experiments. Besides, I would like to thank Jacob and Jinwon in Dr. Matthew Johnston's group. They gave me some good advice in my fabrication process. I would especially like to thank Erwen and Bokun because they have spent a lot of time on teaching and discussing with me.

Finally, I would thank my family for their supports and encouragement.

TABLE OF CONTENTS

Page

1 Introduction 1

1.1 Silicon Photonics 1

1.2 Silicon Microring Resonator and Modulator 1

2 Silicon Passive Device 4

2.1 Silicon Passive Device Fabrication 4

2.2 Silicon Waveguide and Grating Coupler 5

2.2.1 Design and Principle 5

2.2.2 Measurement of Grating Coupler 6

2.3 Silicon Microring Resonator.. 7

2.3.1 Design and Principle 7

2.3.2 Measurement of Microring Resonator 8

2.4 Silicon Subwavelength Microring Resonator 10

2.4.1 Design and Principle 10

2.4.2 Measurement of Subwavelength Microring Resonator 11

3 TCO-Gated MOS Microring Resonator Simulation Setup 13

3.1 Design and Principle 13

3.2 FDE Solver 14

TABLE OF CONTENTS (Continued)

Page

3.3 FDTD Solver 15

3.4 Comparison of Two Simulation Methods 16

4 Silicon Microring Resonator Driven by ITiO Capacitor 18

4.1 Active Device Fabrication 18

4.2 Testing and Measurement 19

4.3 Analysis of Optical Mobility 20

4.4 Further Improvement 22

5 Optimization of Microring Design for High Performance 24

5.1 Improvement from High Mobility TCO Gate 24

5.2 Improvement from Different Structure of Microrings 25

5.2.1 Traditional Microring 25

5.2.2 Subwavelength Microring 27

5.2.3 Slot Microring 29

5.2.4 Comparison 31

6 Conclusion 33

7 Reference 34

LIST OF FIGURES

Figure | Page

1. Fabrication process flow chart for the passive silicon MMR 4

2. Schematic of the grating coupler 6

3. Experimental transmission spectra of the grating couplers 6

4. Schematic of a MMR 8

5. Experimental normalized transmission spectrum of a MMR 9

6. Experimental Q-factor as a function of the gap 9

7. Schematic of SWMR built with trapezoidal silicon blocks 11

8. Simulated transmission of quartered SWMR 11

9. Experimental normalized transmission spectra of the SWMR 12

10. Cross-sectional view of TCO-gated MOS MMR with TCO/oxide/Si MOS structure 14

11. Schematic of FDTD simulation setup 16

12. Comparison between FDE and FDTD solvers 17

13. Optical image of the fabricated ITiO-gated MOS MRR 18

14. Fabrication process flow chart for the silicon active MMR 19

15. Experimental results of ITiO-gated MOS MRR 20

16. Schematic of simulation setup with uniform concentration accumulation........ 21

17. Simulated Q-factor versus free carrier mobility and resonance wavelength shift........ 22

18. Simulation of Q-factor and resonance wavelength shift with 10nm HfO_2 oxide layer 23

LIST OF FIGURES (Continued)

Figure Page

19. Simulated Q-factor and resonance shift with three different TCO materials..............24

20. Simulated resonance shift as a function of wgws...26

21. Simulated Q-factor and the resonance shift with different wgw of traditional MRR .26

22. Simulated electric field intensity ($|E|^2$) distribution of TCO-gated MOS MRR..........27

23. Simulated Q-factor and the resonance shift with different wgws of SWMR..............28

24. Simulated electric field intensity ($|E|^2$) distribution of TCO-gated MOS SWMR 29

25. Simulated Q-factor and resonance shift with different slot width of SLMR 30

26. Simulated electric field intensity ($|E|^2$) distribution of TCO-gated MOS SLWMR....31

LIST OF TABLES

Table Page

1. Summary of different structures of TCO-gated MOS MRR …………………..................... 32

Silicon Microring Resonator Driven by High-Mobility Conductive Oxide Capacitor

1 Introduction

1.1 Silicon Photonics

The network traffic is exponentially increasing as our information and computation technology develop. From 2015 to 2020, the global data center traffic is already grown from 4.7 to 15.3 zettabytes per year [1]. Conventional data transmission with existing electric wiring will not be able to overcome the heavy data traffic soon due to the limitation of the low bandwidth. Instead, optical interconnection, especially silicon photonics, becomes one of the promising photonic integration platforms due to many advantages. First, silicon is transparent to the telecommunication wavelength with ranges in near-infrared and mid-infrared, which can achieve low loss waveguide [2], [3]. Second, unlike most conventional optical devices that are made from III–V-based compounds such as indium phosphide (InP), gallium arsenide (GaAs), or the electro-optic crystal lithium niobate (LiNbO3) [4], silicon photonics is compatible with developed complementary metal-oxide-semiconductor (CMOS) fabrication process. Hence, silicon photonics is showing great potential in large-scale integration with a small footprint, high bandwidth, and low cost.

1.2 Silicon Microring Resonator and Microring Modulator

Among many silicon photonic components, microring resonator (MRR) is unique and popular because of its various application. Many kinds of research have investigated it in MRR, such as all-optical switch [5], sensor [6], modulator [7]. A basic structure of

MRR consists of a straight silicon waveguide and a ring. The details of the MRR will be introduced in chapter 2.

A Silicon microring modulator (MRM) plays a pivotal role in future optical interconnect systems because of the small size and low energy consumption. Most of the existing MRMs are based on reversed PN junctions [8], [9], but they have relatively low electro-optic (E-O) modulation efficiency. The typical reversed PN junction MRM can provide only less than 40 pm/V tunability. To overcome this problem, MRR with an integrated III-V-on-Si metal-oxide-semiconductor (MOS) capacitor demonstrated a much higher E-O efficiency of 55 pm/V [10]. Very recently, an indium-tin-oxide (ITO)-gated MOS MRR has been published, which has high E-O efficiency of 271pm/V [11] using HfO_2 insulator and a narrow microring waveguide. However, the quality factor (Q-factor) is limited to 1000 due to the high optical loss from the ITO gate. In order to improve the Q-factor, high mobility transparent conductive oxide (TCO) materials are preferred since they can significantly reduce the free carrier optical absorption [12]. The principle and simulation setup of TCO-gated MOS MRR will be discussed in chapter 3.

High mobility TCO materials such as titanium-doped In2O3 (ITiO) can experimentally reach 105$cm^2V^{-1}s^{-1}$ by a simple RF sputtering process [13]. In chapter 4, a MRR based on ITiO/SiO2/Si MOS capacitor has been experimentally demonstrated, which achieves an improved Q-factor above 3600 with a big resonance wavelength shift of 450 pm. Besides, a new method has been developed to characterize the optical mobility in the accumulation layer of the MOS structure. At the end of

chapter 4, the analysis shows that a high tunability of 330 pm/V with a high Q-factor greater than 5000 is feasible.

In chapter 5, to further improve the performance of TCO-gated MOS MRR, the different structures of MRRs driven by high mobility conductive oxide capacitor have been compared. The simulation result indicates that an ultra-high tunability of 906 pm/V and a high Q-factor above 6700 can be potentially achieved with slot MRR.

2 Silicon Passive Device

2.1 Silicon Passive Device Fabrication

In this thesis, the devices are fabricated on the silicon on insulator (SOI) wafers, which has a 250 nm silicon top layer and a 3 μm buried oxide layer. Two steps of electron beam lithography (EBL) and reactive ion etching (RIE) processes are applied to get the devices. First, the ZEP520A resist is spin-coated on the top of SOI wafer, and EBL is used to pattern the devices, such as a bus waveguide and a MRR. Using RIE etches 200 nm silicon top layer, and it remains a 50 nm silicon slab, which will be used for the active device (chapter 4). Second, repeat previous steps, using EBL and RIE etches the grating coupler regions, which has a 70 nm etch depth. Figure 1 shows the details of the fabrication process flow chart.

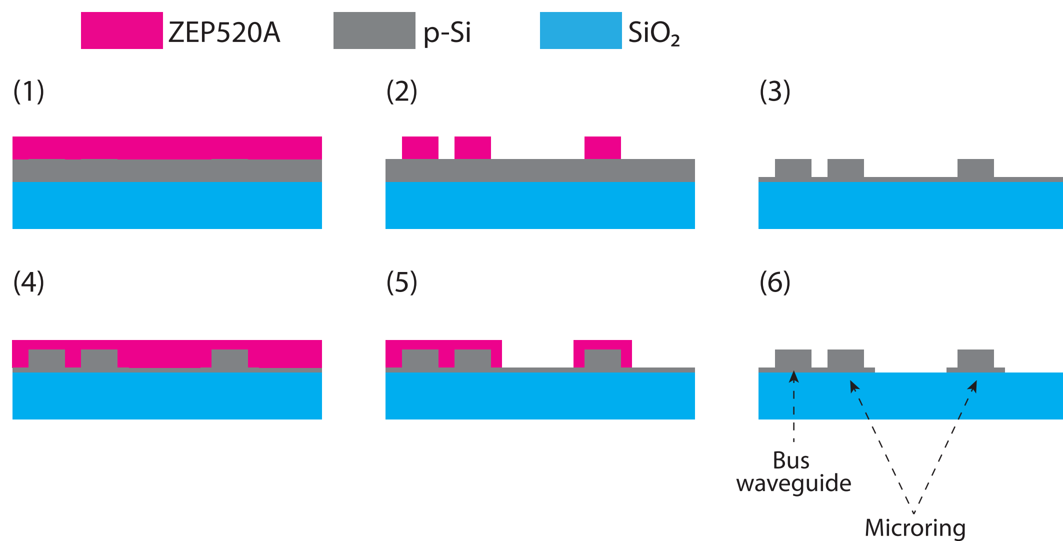

Figure 1: Fabrication process flow chart for the passive silicon MMR. (1) spin resist (2) EBL+Development (3) RIE (4) spin resist (5) EBL+Development (6) RIE

2.2 Silicon Waveguide and Grating Coupler

2.2.1 Design and Principle

SOI wafer can act as an optical fiber, in which the light can propagate in a silicon waveguide. A silicon layer is used as a core, and a buried oxide layer is used as the cladding. For light wavelength at 1550 nm, the refractive index of silicon and silicon dioxide (SiO_2) are 3.467 and 1.444, respectively. Because it has a high index contrast on SOI, it can make a compact footprint with a CMOS fabrication process. Therefore, each chip can consist of a large number of devices.

The thickness of silicon on the SOI wafer is only a few hundred nanometers, so coupling the light from fiber to silicon waveguide is a big challenge. Edge coupling has been used to get high coupling efficiency [14], [15]. However, the devices need to be close to the edge of a wafer, and it has poor tolerance to misalignment. Hence, the grating coupler is one of the popular ways to couple the light into the silicon waveguide, and the fibers can be mounted on the top of the SOI wafer. As Figure 2 shown, the grating is formed with periodically notching the silicon layer, and the grating period can be obtained by [16]:

$$\Lambda = \frac{\lambda_{fr}}{n_{neff-n_{top}\sin\theta}} \tag{1}$$

where Λ is the grating period. λ_{fr} is the free space wavelength. n_{eff} is an effective index. n_{top} is the refractive index of the top cladding. θ is the tilt angle of the fiber.

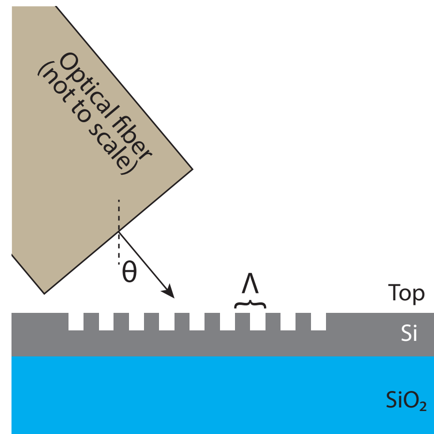

Figure 2: Schematic of the grating coupler

2.2.2 Measurement of Grating Couplers

In the testing setup, the tilt angle of fibers θ is 8°, and figure 3 shows the experimental transmission spectra with a different granting period. The fiber to fiber coupling efficiency is around -16 dB. When the period is at 590 nm, the center of wavelength is at 1550 nm, which is the telecommunication wavelength that commonly used.

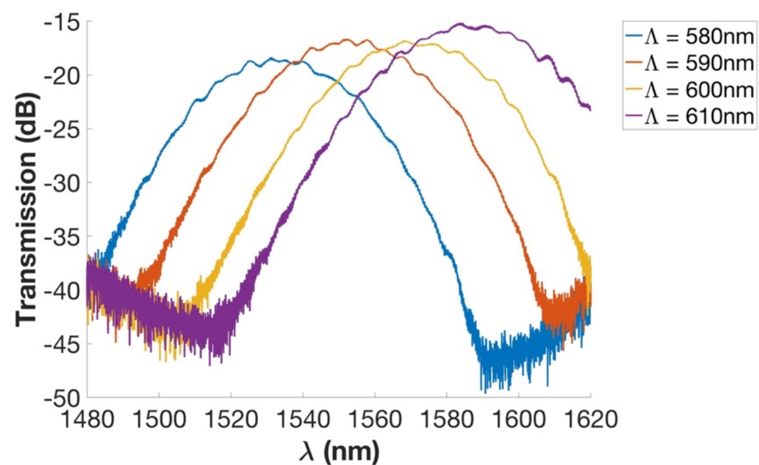

Figure 3: Experimental transmission spectra of the grating couplers with different periods and a waveguide width of 400.

2.3 Silicon Microring Resonator

2.3.1 Design and Principle

As figure 4 shown, a MRR consists of a straight bus waveguide and a loop optical waveguide, which is a ring shape. Since it is a resonator, when the optical wave in the looped waveguide has a phase shift that equals 2π times an integer, it has a resonance. In other words, the resonance wavelength

$$\lambda_{res} = \frac{n_{neff}L}{m},\ m = 1,2,3\ldots \tag{1}$$

where λ_{res} is the resonance wavelength. n_{eff} is an effective index. L is the circumference of a ring.

The quality factor (Q-factor) is used to determine the sharpness of the resonance:

$$Q - factor = \frac{\lambda_{res}}{FWHM} \tag{2}$$

where FWHM is full width at half maximum.

The Q-factor depends on not only the loss of the resonator but also the coupling between the bus waveguide and the ring. Therefore, the gap between the bus waveguide and the ring is also critical in the design. When the gap is too small, the ring is over coupling. In contrast, when the gap is too large, the ring is under coupling. In both over coupling and under coupling, the intensity trough is not as deep as in the critical coupling [17]. In critical coupling, the transmission at resonance wavelength decreases

to zero, so the highest Q-factor happens at this condition. Therefore, the critical coupling can be achieved by adjusting the gap between a straight waveguide and a ring.

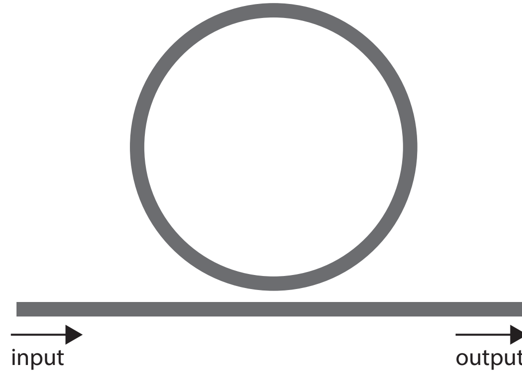

Figure 4: Schematic of a MMR. It consists of a straight waveguide and a ring waveguide.

2.3.2 Measurement of Microring Resonator

In order to be at critical coupling, the MRRs have fabricated with several different gaps on the same SOI wafer. The MRR has a radius of 6 μm and a waveguide width (wgw) of 400 nm. Figure 5 shows the normalized transmission spectrum of the measurement, and the Q-factor can be determined by equation (2). Figure 6 shows the changes in Q-factor by adjusting the gaps. When the gap is 250nm, it has the highest Q-factor of 20k. However, when the gaps are larger or smaller than 250nm, the Q-factors starts to decrease. This experimental result clearly explains that critical coupling plays an essential role in getting high Q-factor.

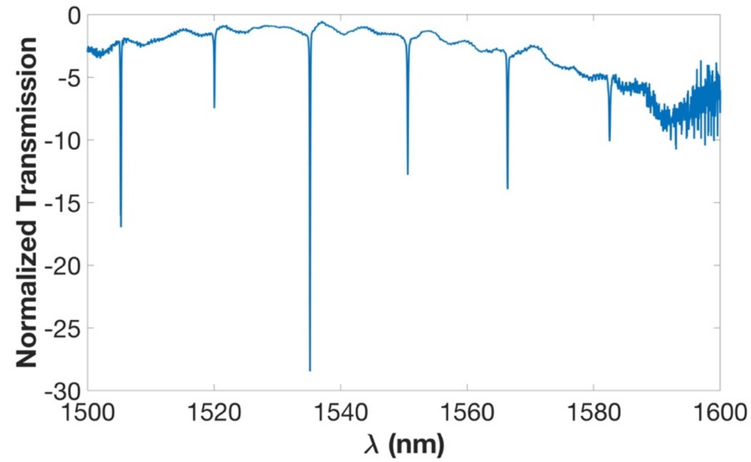

Figure 5: Experimental normalized transmission spectrum of a MMR with a radius of 6 μm and a wgw of 400 nm

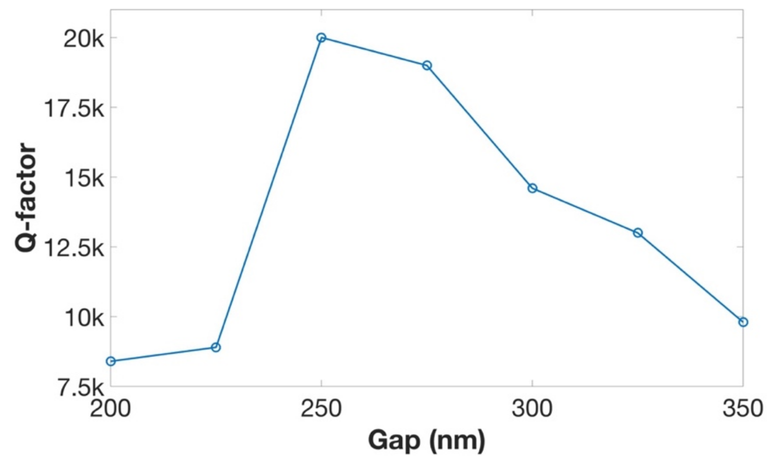

Figure 6: Experimental Q-factor as a function of the gap. A microring resonator has a radius of 6 μm and a wgw of 400 nm. It sweeps gaps to get the critical coupling condition.

2.4 Silicon Subwavelength Microring Resonator

2.4.1 Design and Principle

One more design is combining MRR with subwavelength grating, called subwavelength microring resonator (SWMR). SWMRs have been widely used for optical sensing [18]–[20]. A subwavelength grating consists of periodically arranged dielectric particles with dimensions much smaller than the wavelength [21]. However, the conventional rectangular silicon SWMR has a high bending loss, so using trapezoidal silicon blocks can reduce the loss [22]. Furthermore, using trapezoidal shape SWMR to improve Q-factor has been published [18], [19].

Since Q-factor depends on the loss of a ring, low bending loss is needed for the high Q-factor. Besides, the geometry of the silicon block affects the bending loss of a ring so it can get a high Q-factor by optimizing the size of the silicon block. FDTD solver, which will be introduced more details in chapter 3.3, is used to sweep the L_{in} and L_{out} of the trapezoid to get the high transmission (low bending loss), as figure 7 shown.

In order to reduce the bending loss, the radius of SWMR is increased to 8 μm. Figure 8 shows the simulated transmission result of quartered SWMR. Too larger L_{in} (or L_{out}) is not considered because the SWMR needs to have enough gaps between each silicon blocks to make it as an active device in the future. The black star in figure 8(a) indicates that the SWMR with a wgw of 450 nm and L_{out}/L_{in} of 180 nm/220 has a simulated Q-factor of 1100 by the calculation of simulated transmission. To further improve the Q-factor, Figure 8(b) shows the SWMR with a wgw to 650 nm, and L_{out}/L_{in} of 120 nm/210 nm has a simulated Q-factor of 7400, which is indicated by a black star.

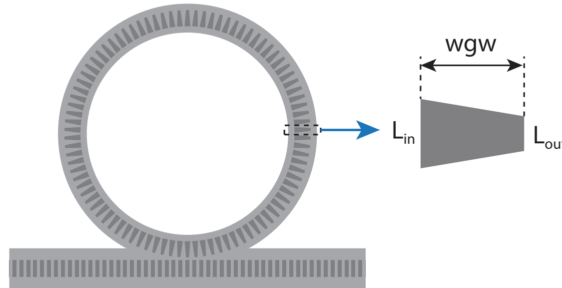

Figure 7: Schematic of SWMR built with trapezoidal silicon blocks

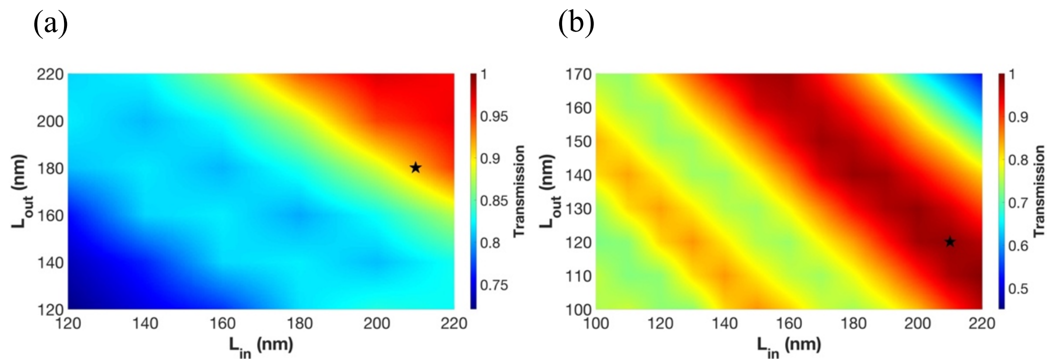

Figure 8: Simulated transmission of quartered SWMR with a period of 300 nm and a radius of 8 μm. The black stars indicate the conditions with high Q-factors and suitable gaps for active devices. A SWMR has a wgw of (a) 450 nm (b) 650 nm.

2.4.2 Measurement of Subwavelength Microring Resonator

The two different SWMRs have been fabricated on SOI wafers. Figure 9 shows the experimental normalized transmission spectra of the SWMR with a radius of 8 μm and a period of 300nm. A SWMR with a wgw of 450 nm has an experimental Q-factor of 710, and a SWMR with 650 nm has the experimental Q-factor of 5400.

The experimental Q-factors are lower than the expected Q-factors. Simulation results show the Q-factor is very sensitive to the geometry of the silicon block even though it only has a 10 nm difference. For example, at a wgw of 650 nm, when the

L_{out}/L_{in} is at 120 nm/210 nm, it has a high simulated Q-factor of 7400. However, if it only reduces L_{in} from 210 nm to 200 nm, the simulated Q-factor will decrease to 4000, and the small error might happen in the fabrication process. Therefore, the SWMR can potentially obtain a high Q-factor of 7400 by optimizing the fabrication process.

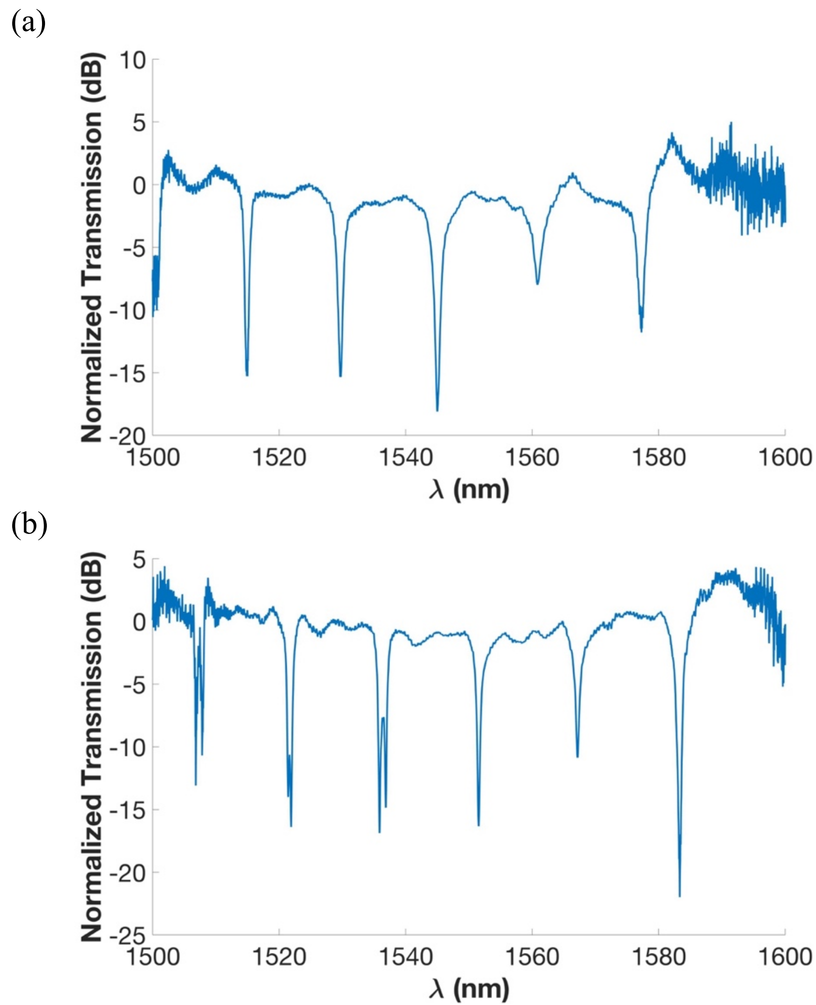

Figure 9: Experimental normalized transmission spectra of the SWMR with a radius of 8 μm and a period of 300nm. (a) A SWMR has a waveguide width of (a) 450 nm (b) 650 nm.

3 TCO-Gated MOS Microring Resonator Simulation Setup

3.1 Design and Principle

In this chapter, the tunable MRR is designed with a MOS capacitor, which consists of a TCO layer, an oxide layer, and silicon. As figure 10 shown, applying a negative bias on the TCO gate induces free carrier accumulation. Electrons accumulate in the TCO layer, and holes accumulate in the p-type silicon layer.

The behavior of the devices can be described by the Drude model [23]:

$$\varepsilon(\omega) = \varepsilon_\infty - \frac{\omega_p^2}{\omega(\omega+i\Gamma)} \quad (1)$$

where ε_∞ is the high frequency dielectric constant, Γ is a damping frequency, and

$$\omega_p^2 = \frac{N_c q^2}{\varepsilon_0 m^*} \quad (2)$$

where N_c is the free carrier concentration, q is the electron charge, ε_0 is the permittivity of free space, and m^* is the electron effective mass.

As the free carrier concentration N_c increasing, the permittivity decreases, and it causes the reduction of the refractive index. Besides, the resonance wavelength depends on the effective index (chapter 2.2.1), so the resonance wavelength has a blue shift when a negative bias applies.

In TCO-gated MOS MRR, two simulation methods are used. One is finite-difference-eigenmode (FDE) solver in Lumerical MODE software, and the other one is the 3D-finite-difference-time-domain (FDTD) solver in Lumerical FDTD software.

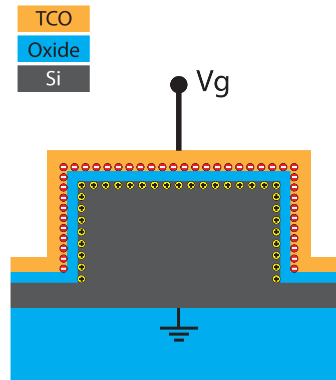

Figure 10: Cross-sectional view of TCO-gated MOS MMR with TCO/oxide/Si MOS structure. When a negative bias is applied, electrons and holes accumulate at TCO/oxide and Si/oxide interfaces, respectively.

3.2 FDE Solver

For FDE solver, the quantum model is applied [24]. The free carrier concentration distribution with different applied negative bias in the accumulation layer is imported from Silvaco, and the loss of bent waveguide and effective index can be simulated. The resonance shift can be calculated by:

$$\Delta\lambda = \frac{\Delta n_{eff}}{n_{eff}} \lambda_{res} \tag{3}$$

where n_{eff} is the effective index, and λ_{res} is the resonance wavelength.

The Q-factor can be calculated from the loss with [25]:

$$Q - factor = \frac{\pi n_g L\sqrt{ra}}{\lambda_{res}(1-ra)} \tag{4}$$

where a is the single-pass amplitude transmission, which is related to the loss α [1/cm] as $a^2 = \exp(-\alpha L)$. r is the self-coupling coefficient. L is the circumference of a ring. n_g is the group index.

3.3 FDTD Solver

For FDTD solver, due to the time consumption about computing and the memory limitation of hardware, the free carrier concentration distribution cannot be imported into FDTD because it needs an extremely fine mesh. Therefore, a uniform concentration model is applied [24]. Since the permittivity change caused by the plasma dispersion is proportional to the change of free-carrier concentration, namely, $\Delta\varepsilon \propto \Delta N_c$ [26]. The free carrier concentration is still imported from Silvaco, and total accumulated free carriers induced by different applied voltages can be obtained by integral. Finally, the total accumulated free carriers are uniformly distributed on the entire TCO layer.

Figure 11 shows that it simulates only a quarter of the microring. The single-pass amplitude transmission can be calculated from:

$$a = \left(\frac{I_{out}}{I_{in}}\right)^2 \tag{5}$$

where I_{out}/I_{in} is the transmission of quartered microring. Therefore, Q-factor can be calculated with equations (4) and (5).

The electric field and permittivity are exported from Lumerical, and the resonance shift can be calculated by [27]:

$$\Delta\omega = -\frac{\omega}{2}\frac{\int \Delta\varepsilon|E|^2 dv}{\int \varepsilon|E|^2 dv} \quad (6)$$

where E and ε are electric field and permittivity, respectively.

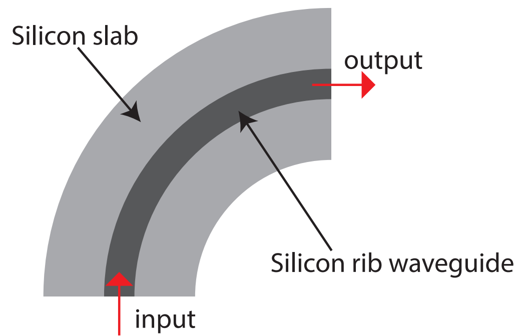

Figure 11: Schematic of FDTD simulation setup. It simulates the transmission of the quartered bent waveguide.

3.4 Comparison of two simulation methods

In chapter 3.2 and 3.3, two simulation methods are introduced. In this chapter, the same device will be simulated by FDE and FDTD solvers. In the simulations, the MRR consists of a radius of 6 μm and a wgw of 400 nm. Besides, it has a waveguide height of 250 nm and a slab height of 50 nm. The TCO-gated MOS MRR has a 10 nm thick HfO_2 oxide layer and a 10 nm thick TCO layer. In the simulations, a cadmium oxide (CdO) is used for the TCO material, which has mobility of 300 $cm^2V^{-1}s^{-1}$ [12]. Besides, the doping levels of p-Si and CdO used in the simulation are 1×10^{17} and 1×10^{19} cm^{-3},

respectively. Figure 12 shows that FDE solver (solid lines) and FDTD (dashed lines) have close results, which errors are within 7%.

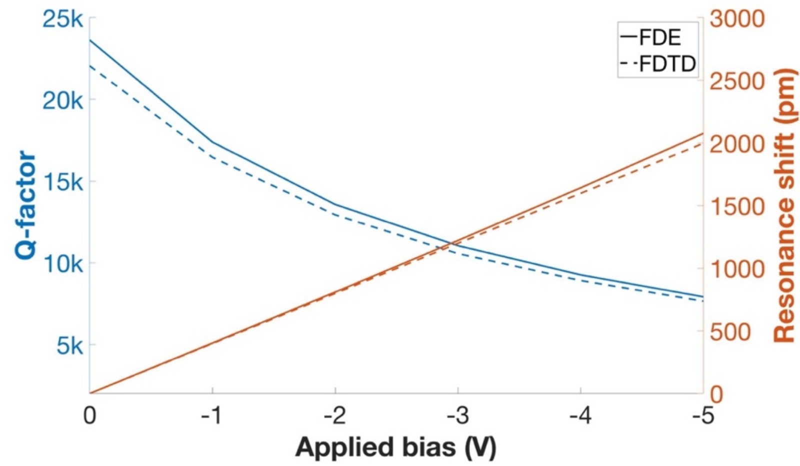

Figure 12: Comparison between FDE and FDTD solvers. FDE solver (solid lines) and FDTD solver (dashed lines). Simulated Q-factor (blue lines, left y-axis) and resonance shift (red lines, right y-axis).

4 Silicon microring resonator driven by TCO capacitor

4.1 Active Device Fabrication

In this chapter, the tunable silicon MRR is designed with a MOS capacitor, which consists of ITiO, SiO_2, and silicon. The device has been fabricated on a SOI wafer. First, passive MRR follows the same fabrication process, which is mentioned in chapter 2.2.1. It consists of a radius of 6 µm and a wgw of 400 nm, Next, an 18 nm thick SiO_2 layer is formed by dry oxidation at 1000°C. The SiO_2 on the silicon contact region is etched by hydrofluoric (HF) acid. Then, 17 nm ITiO is deposited by RF sputtering, followed by a liftoff process and patterned by EBL with the resist ZEP520A. The ITiO gate is deposited by RF-sputtering, which has a mobility of 26 $cm^2V^{-1}s^{-1}$ measured by Hall measurement. Finally, the Ni/Au electrodes are thermally evaporated and patterned by regular photolithography. The top view of the fabricated ITiO-gated MRR is shown in figure 13, and the fabrication process flow chart is shown in figure 14.

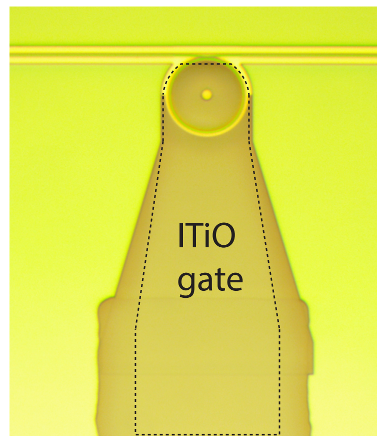

Figure 13: Optical image of the fabricated ITiO-gated MOS MRR. The ITiO gate, which is highlighted by the black dashed line, covers the active region of the microring except the coupling region to the bus waveguide.

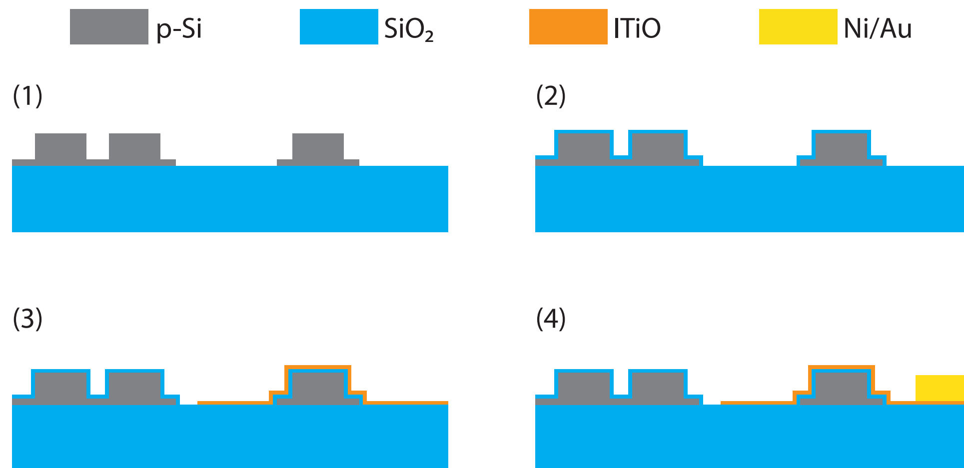

Figure 14: Fabrication process flow chart for the silicon active MMR. (1) silicon passive MMR (2) Thermal oxidation (3) RF sputtering followed by a liftoff process and contact region is etched by HF acid (4) Thermal evaporation

4.2 Measurement of Microring Modulator

Figure 15(a) shows the experimental spectra of the normalized transmission with different negative biases. Q-factor and resonance wavelength shift as a function of the applied bias is plotted in figure 15(b) that the solid lines represent the experimental result, and the dashed lines represent the simulated result. When the applied bias is beyond -2V, the resonance shift is almost linearly proportional to the applied bias, and it has an average wavelength tunability of 42 pm/V, which is very close to the simulated tunability of 45 pm/V. The Q-factor is still higher than 3600 when it has a cumulative resonance wavelength shift of 450pm. Experimental and simulation Q-factors have errors within 3%.

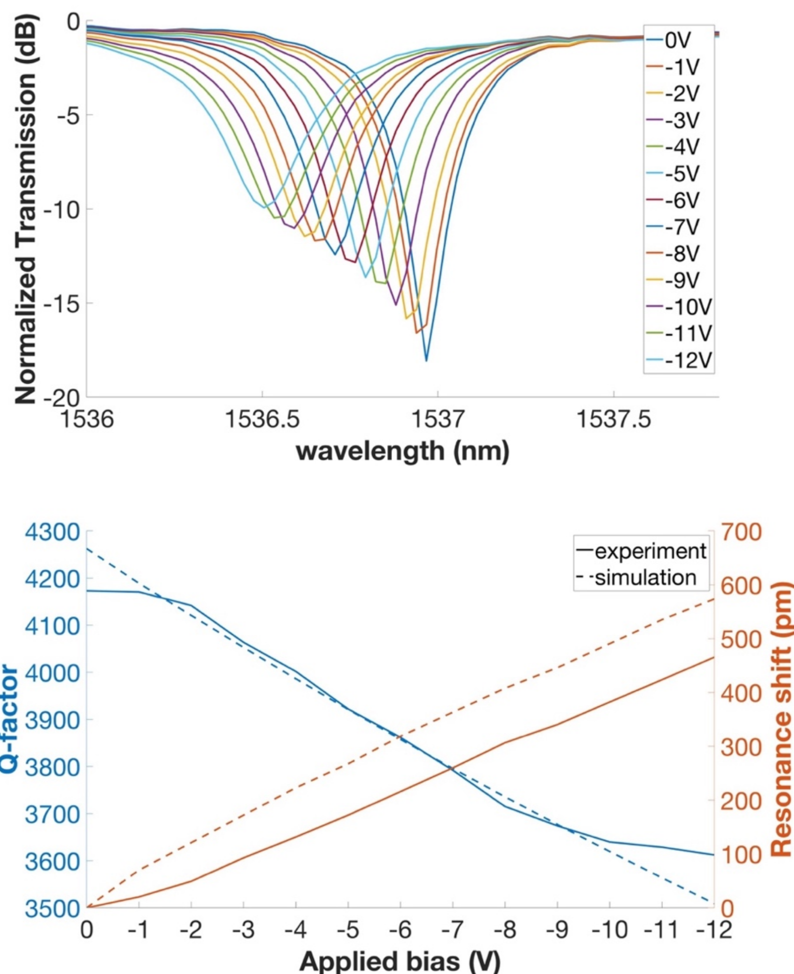

Figure 15: Experimental results of ITiO-gated MOS MRR. (a) Normalized transmission spectra with different gate biases. (b) Experimental and Simulated results with a mobility of 26 $cm^2V^{-1}s^{-1}$. Experimental Q-factor (solid blue line, left y-axis) and resonance shift (solid red line, right y-axis). Simulated Q-factor (blue dashed line, left y-axis) and resonance shift (red dashed line, right y-axis).

4.3 Analysis of Optical Mobility

In figure 15(b), the experimental Q-factor degrades more slowly after -8V. Since the device is operated in accumulation mode, understanding the optical properties of the material in the accumulation layer is essential. The ellipsometry with the Drude model

has been used commonly to estimate optical mobility. However, it is susceptible to surface imperfections [28], so the optical mobility may not be accurate by ellipsometry for thin film, especially in the accumulation layer. Therefore, a new method has been designed to estimate optical mobility in the accumulation layer.

First, FDE solver (chapter 3.2) is used in this simulation setup, and a uniform concentration model is applied. Since the TCO-gated MOS MRR is operated in accumulation mode, so when a negative bias is applied, it induces the accumulation layer. As figure 16 shown, the uniform concentration accumulation (Nacc) layer is designed as 1nm [24] in this simulation.

The Q-factor and resonance shift are simulated by changing Nacc and mobilities in the 1nm accumulation layer. Figure 17 shows the simulated Q-factor with respect to the free carrier mobility and the resonance wavelength shift. The experimental resonance shift and Q-factor are used to derive the in-device optical mobility, and it shows a trend of increasing mobility as the gate bias increases.

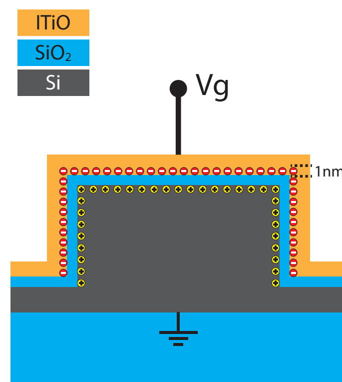

Figure 16: Schematic of the simulation setup with uniform concentration accumulation. The accumulation layer is induced when a negative bias is applied to the ITiO gate. Assume the accumulation layer thickness is 1 nm.

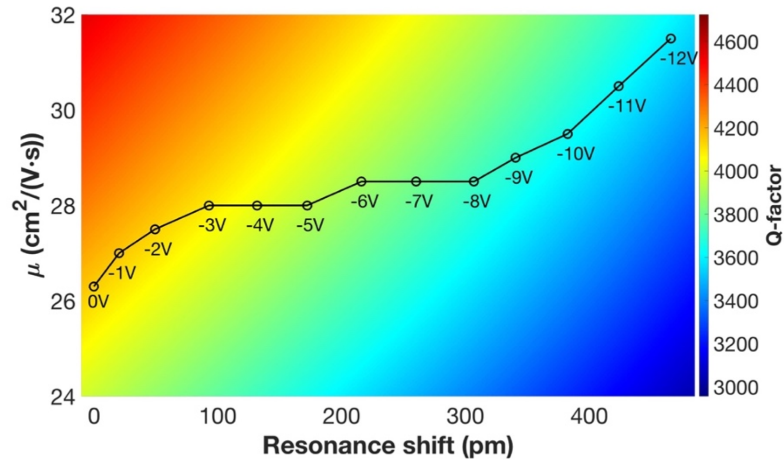

Figure 17: Simulated Q-factor versus free carrier mobility and resonance wavelength shift.

4.4 Further Improvement

To further improve the device performance, A mobility of 66 $cm^2V^{-1}s^{-1}$ was achieved by adding substrate heating at 450°C during the ITiO sputtering process in our RF sputtering tool. However, this high temperature causes decomposition of the resist in the liftoff process. RIE is planning to be used instead of the liftoff process for the fabrication of the ITiO-gated MOS MRR. Moreover, the resonance wavelength shift is proportional to the capacitance per unit active volume [26], so the wavelength tunability can be improved by replacing the 18nm SiO_2 with 10nm HfO_2 oxide layer. Figure 18 shows the simulated result that it will achieve a high wavelength tunability and a high Q-factor with high mobility ITiO. It has a high wavelength tunability of 330 pm/V, and the Q-factor will still be greater than 5000 even when it has a resonance shift of 1.3nm.

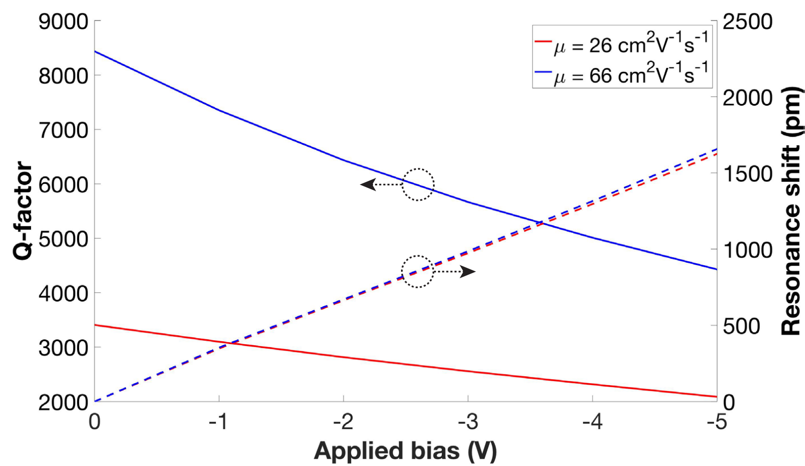

Figure 18: Simulation of Q-factor and resonance wavelength shift with 10nm HfO_2 oxide layer: comparison between different free carrier mobilities. Q-factor (solid line, left y-axis) and resonance shift (dashed line, right y-axis) as a function of applied gate bias.

5 Optimization of Microring Design for High Performance

5.1 Improvement from High mobility TCO Gate

There are various TCO materials have been published. For example, ITO has mobility around 25 $cm^2V^{-1}s^{-1}$ [29]. ITiO has a mobility around 100 $cm^2V^{-1}s^{-1}$ [13]. CdO has a mobility around 300 $cm^2V^{-1}s^{-1}$ [12]. In order to further improve the performance of TCO-gated MOS MRR, high mobility TCO materials are preferred since they can significantly reduce the free carrier optical absorption [12].

In chapter 5.1, the FDE solver is used for comparing the performance of microring modulator with different mobilities TCO materials. Figure 19 shows the simulation results with different mobilities TCO materials. This simulation clearly confirmed the significance of high mobility TCO materials.

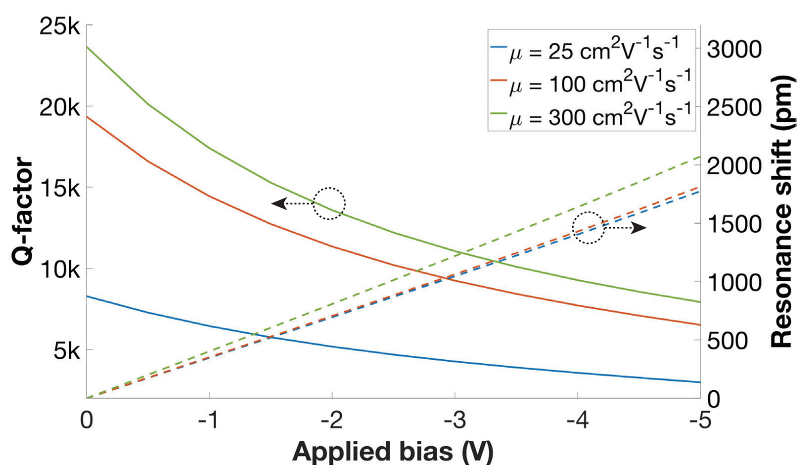

Figure 19: Simulated Q-factor and resonance shift with three different TCO materials. Q-factor (solid line, left y-axis) and resonance shift (dashed line, right y-axis) as a function of applied gate bias.

5.2 Improvement from Different Structure of Microrings

High mobility TCO materials can further improve Q-factors as a result of chapter 5.1. Not only Q-factor but also the resonance shift can be enhanced to achieve high performance. As chapter 4.4 mentioned, the resonance shift can be increased by using a 10 nm HfO2 oxide layer. Therefore, the 10nm CdO layer, which has a high mobility of 300 cm2V-1s-1 and a 10 nm HfO2 oxide layer, will be applied in chapter 5.2 to achieve better Q-factors and the resonance shift. Besides, different structures of MMRs will be compared in this chapter.

5.2.1 Traditional Microring Resonator

The MRR (Traditional MMR) has been widely used, and it is also discussed in previous chapters. From equation (6), the resonance shift depends on the change of permittivity and electric field intensity, so increasing the overlapping factor with the TCO layer will help the TCO-gated MOS MRR to improve the resonance shift. Therefore, the resonance shift can be enhanced by optimizing wgws. Figure 20 shows the resonance shift as a function of wgw at -1V. At a wgw of 300 nm, it can achieve the highest resonance shift.

In previous chapters, only the wgw of 400 nm is used for MRR. Figure 21 shows the TCO-gated MOS MRR with a wgw of 300 nm can achieve a high resonance shift of 562.5 pm/V. Since it is using CdO as the gate material, which has high mobility, it remains a Q-factor of 8000 after the 2nm resonance shift. Besides, figure 22 shows the cross-sectional view of the mode profile of MRR with wgws of 300 and 400 nm.

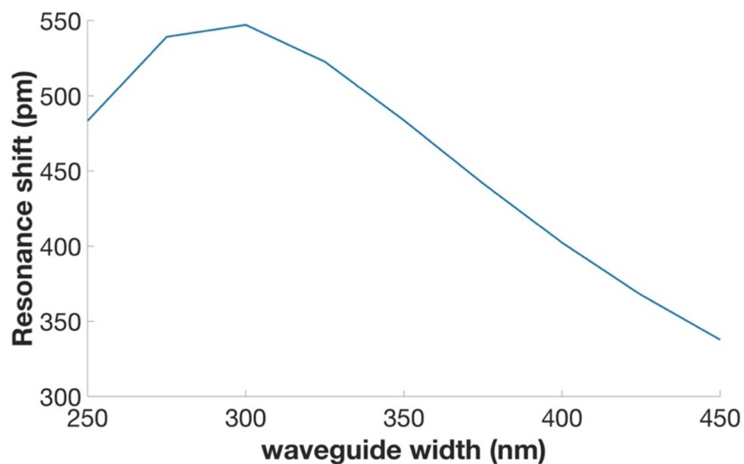

Figure 20: Simulated resonance shift as a function of wgw when -1V bias is applied.

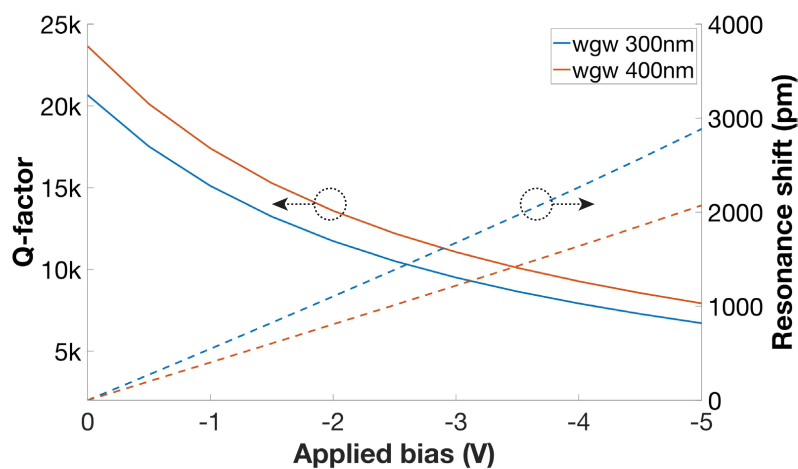

Figure 21: Simulated Q-factor and the resonance shift with different wgw of traditional MRR. Q-factor (solid line, left y-axis) and resonance shift (dashed line, right y-axis) as a function of applied gate bias.

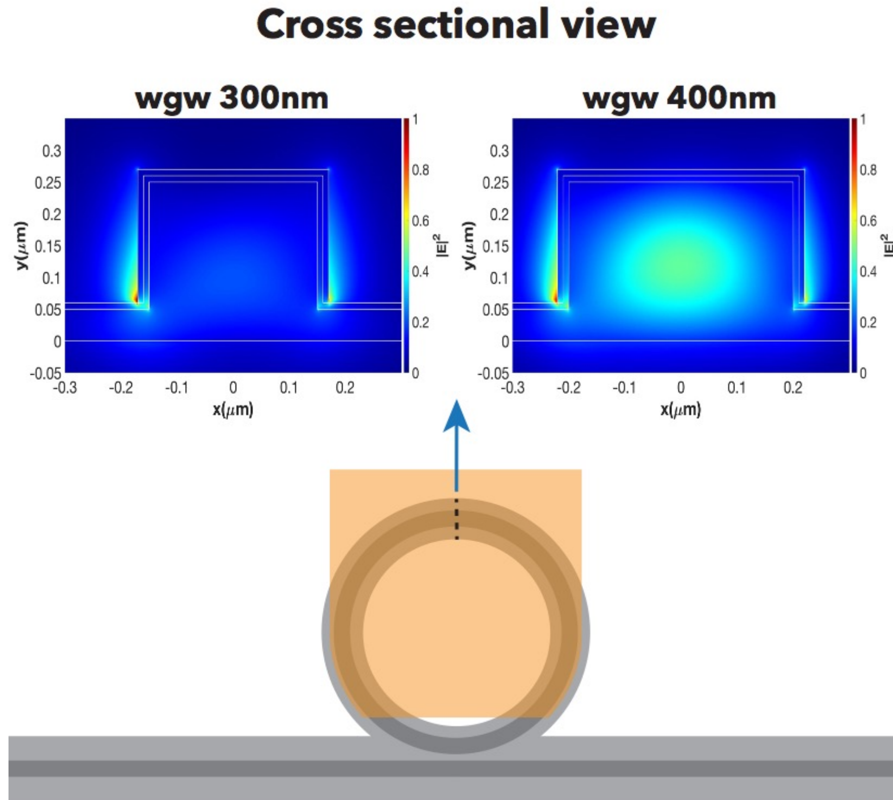

Figure 22: Simulated cross-sectional electric field intensity ($|E|^2$) distribution of TCO-gated MOS MRR with wgws of 300 and 400 nm.

5.2.2 Subwavelength Microring Resonator

As the discussion in chapter 2.4, SWMR has been widely used for optical sensing, and it consists of periodically arranged silicon blocks. This feature of SWMR can be a benefit for improving the overlapping factor because TCO materials can be filled in the gaps between each silicon blocks. Therefore, it will have more overlapping with TCO layers. Since the oxide and TCO layers will be put on each silicon block, and the geometry of each block will influence the bending loss of the grating waveguide. In order to get a better Q-factor, we have used the FDTD solver to re-sweep the size of

each block with HfO_2 and CdO layers. Finally, each silicon block has a wgw of 650 nm and L_{out}/L_{in} 150/220 nm. Also, the period of the grating waveguide is 280 nm.

Besides, as chapter 5.2.1 mentioned, the overlapping factor can be improved by reducing the wgw for traditional MRR, so we have designed the other SWMR that each silicon block has a wgw of 500 nm, L_{out}/L_{in} of 170/220 nm.

Figure 23 shows the simulation results of the two different wgws. Both designs can achieve a higher resonance shift than the traditional MRR because of the improvement from the overlapping factor. A wgw of 650 nm has a lower propagation loss, so the Q-factor is higher than a waveguide width of 500 nm. However, the resonance shift between these two designs does not have a big difference. Figure 24 shows the top view of mode profiles of TCO-gated MOS SWMR, and the mode of both designs is mostly concentrated on the inner radius, so the resonance shift does not have significant improvement by optimizing the wgw.

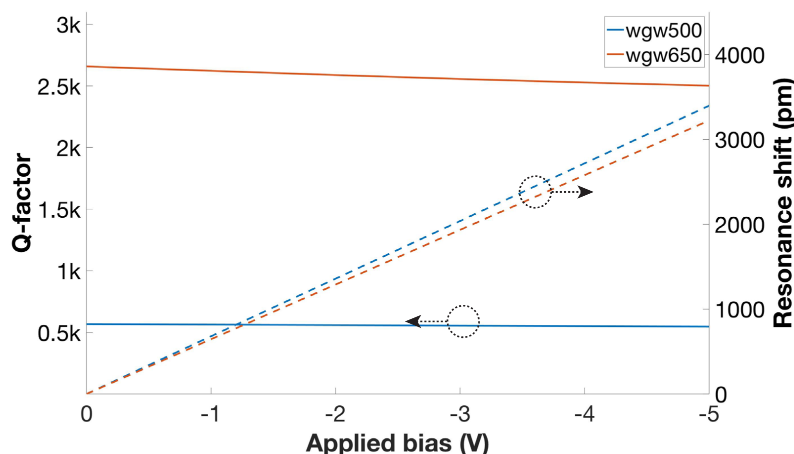

Figure 23: Simulated Q-factor and the resonance shift with different wgws of SWMR. Q-factor (solid line, left y-axis) and resonance shift (dashed line, right y-axis) as a function of applied gate bias

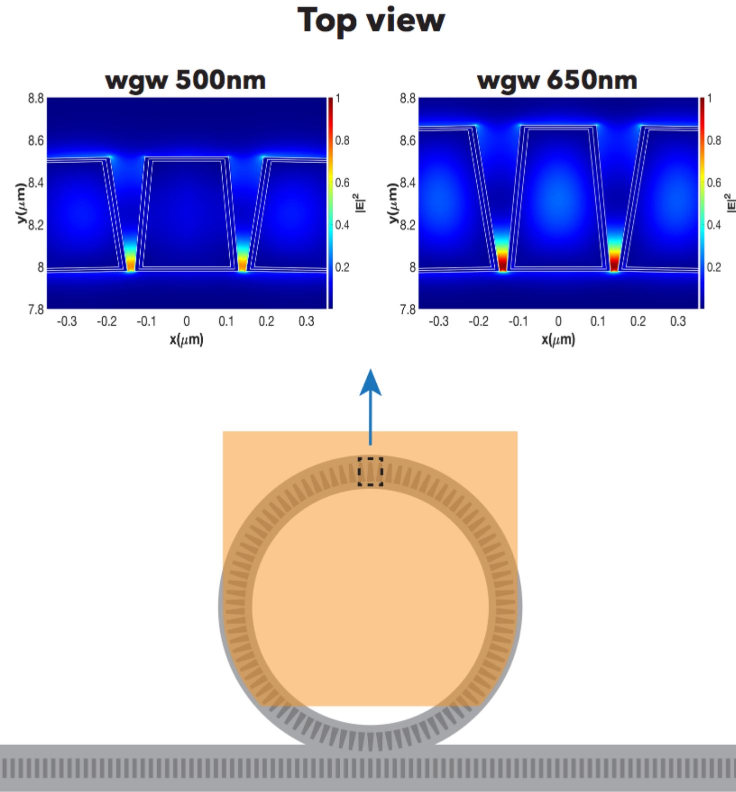

Figure 24: Simulated top view of electric field intensity ($|E|^2$) distribution of TCO-gated MOS SWMRR

5.2.3 Slot Microring Resonator

The other popular design for optical sensing is the slot waveguide. Silicon slot waveguide and slot microring resonator (SLMR) have also been widely used for optical sensing [30]–[34]. SLMR can be used to achieve a high resonance shift, and the principle is similar to SWMR, as chapter 5.2.2 mentioned. The overlapping factor can be improved by filling TCO materials into the gap between silicon waveguides. The wgw is fixed at 450 nm to keep a high Q-factor because the wider wgw can reduce the propagation loss. Two different slot widths between the silicon waveguides, which are

60 nm and 120 nm, are compared in this simulation. Figure 25 shows the simulation result of varying slot widths. When the waveguide has a slot width of 60nm, it has an ultra-high tunability of 906.7 pm/V. It still can keep a high Q-factor above 6700 after a 2 nm resonance shift. Figure 26 shows the cross-sectional mode profile of TCO-gated MOS SLMR. Most of the mode is concentrated at the slot region, so when the slot is smaller, it can get a better overlapping factor. Hence, a smaller slot can improve the resonance shift.

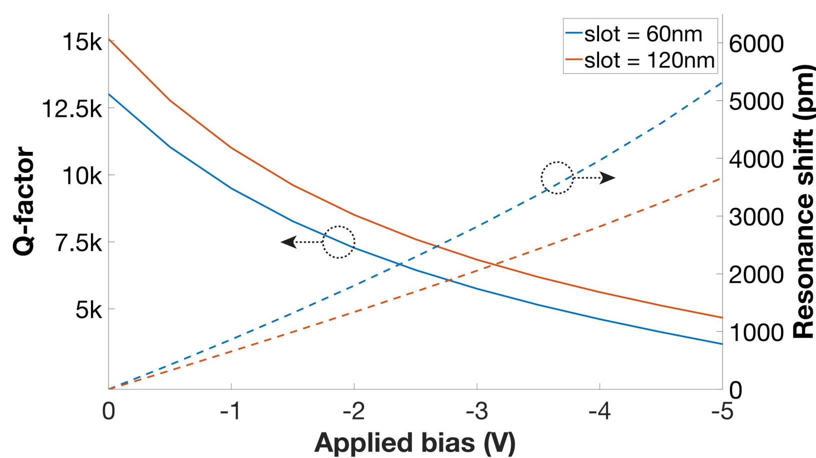

Figure 25: Simulated Q-factor and resonance shift with different slot width of SLMR. Q-factor (solid line, left y-axis) and resonance shift (dashed line, right y-axis) as a function of applied gate bias.

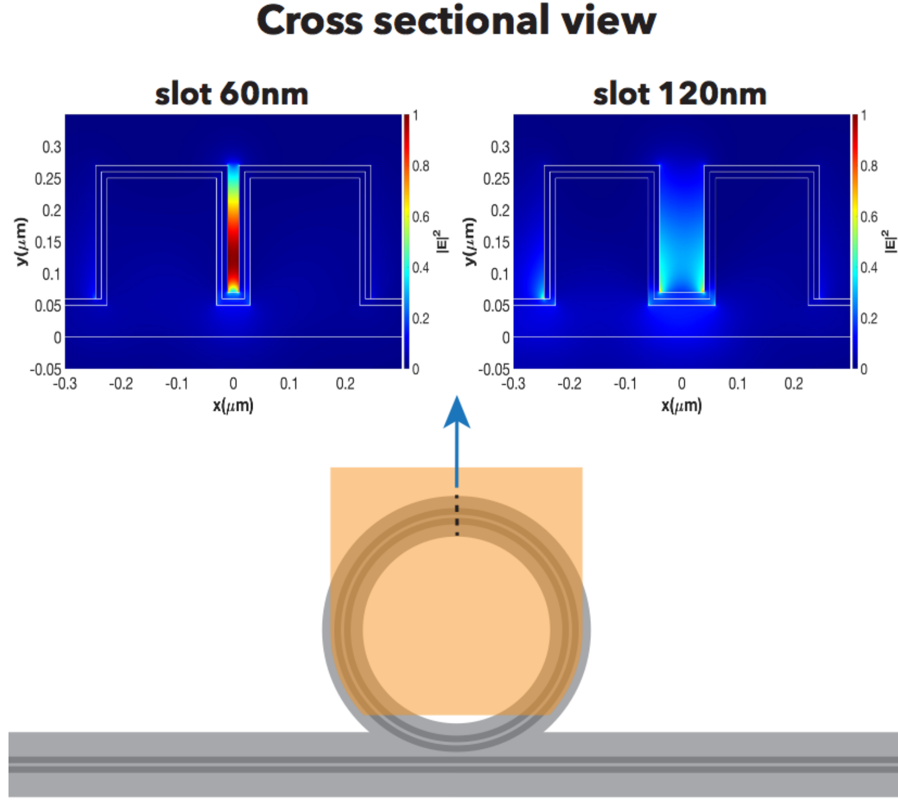

Figure 26: Simulated cross-sectional electric field intensity ($|E|^2$) distribution of TCO-gated MOS SLMR with slots of 60 and 120 nm.

5.2.4 Comparison

Three different structures of microring resonators for E-O modulator have been compared in chapter 5.2.1 to 5.2.3. Ideally, the performance needs both high Q-factor and high resonance shift. However, simulation results show there is a tradeoff between Q-factor and the resonance shift. Here, a figure of merit is defined to determine the performance:

$$\mathrm{FOM} = \mathrm{Q_{2nm}} \times \mathrm{Tunability_{2nm}}\left(\frac{\mathrm{pm}}{\mathrm{V}}\right) \times 10^{-6}\,\left(\frac{\mathrm{V}}{\mathrm{pm}}\right) \tag{7}$$

where Q_{2nm} is the remained Q-factor after the 2nm resonance shift. $Tunability_{2nm}$ is defined as 2000 pm divided by the applied bias V_{2nm} that can make 2000 pm resonance shift.

Table 1 shows a summary of all structures that we have discussed in chapter 5.2. Traditional MMR has the highest Q-factor, but the tunability is relatively low. SWMR improves tunability by increasing the overlapping factor with the TCO layer. However, SWMR has a very low Q-factor even it can achieve a high tunability. SLMR has a higher tunability with a high Q-factor. Overall, SLMR has the FOM in these three designs; it can make not only a high Q-factor but also an ultra-high tunability.

Design		**V_{2nm} (V)**	**Q_{2nm}**	**$Tunability_{2nm}$ (pm/V)**	**FOM**
Traditional Microring	wgw300nm	-3.6	8001.2	562.5	4.5
	wgw400nm	-4.8	8349.1	413.7	3.5
Subwavelength Microring	wgw500nm	-2.9	558.9	679.4	0.4
	wgw650nm	-3.1	2531.1	644.6	1.6
Slot Microring	slot60nm	-2.2	6788.7	906.7	6.2
	slot120nm	-2.9	7482.3	683.6	5.1

Table 1. Summary of different structures of TCO-gated MOS MRR. V_{2nm} is the applied bias that can make resonance wavelength shift 2nm. Q_{2nm} is the remained Q-factor after the 2nm resonance shift. Tunability2nm is the average resonance shift per volt at V_{2nm}.

6 Conclusion

In conclusion, a passive MRR with a high Q-factor of 20,000 is fabricated in this thesis, and a passive SWMR can potentially obtain a high Q-factor of 7400 by optimizing the fabrication process. Next, an ITiO-gated MOS MRR has been demonstrated to get a tunability of 42 pm/V with a high Q-factor above 3,600. With this structure and the simulation, a new method has been developed to characterize the optical frequency free carrier mobility in the accumulation layer of the MOS structure. In the last chapter, different MRRs driven by high mobility TCO materials are compared. The Q-factor can be improved by using high mobility TCO materials, and the resonance shift can be increase by optimizing different structures of MRRs. The simulation results indicate that an ultra-high tunability of 906 pm/V and a high Q-factor above 6,700 can be potentially achieved with SLMR.

7 Reference

[1] T. Barnett Jr. and A. Sumit, “Cisco Global Cloud Index 2015–2020,” *Cisco Knowl. Netw. Sess.*, no. November 2016, 2016, [Online]. Available: https://www.cisco.com/c/dam/m/en_us/service-provider/ciscoknowledgenetwork/files/622_11_15-16-Cisco_GCI_CKN_2015-2020_AMER_EMEAR_NOV2016.pdf?dtid=osscdc000283.

[2] R. Shankar and M. Lončar, “Silicon photonic devices for mid-infrared Applications,” *Nanophotonics*, vol. 3, no. 4–5, pp. 329–341, 2014, doi: 10.1515/nanoph-2013-0027.

[3] J. Wang *et al.*, “A silicon-on-insulator polarization diversity scheme in the mid-infrared,” *Opt. Express*, vol. 23, no. 11, p. 15029, 2015, doi: 10.1364/oe.23.015029.

[4] A. Reed, Graham Knights, “Silicon Photonics - an Introduction,” *J. Chem. Inf. Model.*, vol. 53, pp. 1689–1699, 2013, doi: 10.1017/CBO9781107415324.004.

[5] V. R. Almeida, C. A. Barrios, R. R. Panepucci, and M. Lipson, “All-optical control of light on a silicon chip,” *Nature*, vol. 431, no. 7012, pp. 1081–1084, 2004, doi: 10.1038/nature02921.

[6] M. K. Park *et al.*, “Label-free aptamer sensor based on silicon microring resonators,” *Sensors Actuators, B Chem.*, vol. 176, pp. 552–559, 2013, doi: 10.1016/j.snb.2012.08.078.

[7] Q. Xu, S. Manipatruni, B. Schmidt, J. Shakya, and M. Lipson, “Ring Silicon Modulators,” *Opt. Express*, vol. 15, no. 2, pp. 430–436, 2007.

[8] P. Dong, S. Liao, D. Feng, H. Liang, and D. Zheng, “silicon electro-optic modulator,” vol. 17, no. 25, pp. 22484–22490, 2009.

[9] X. Xiao *et al.*, “25 Gbit/s silicon microring modulator based on misalignment-tolerant interleaved PN junctions,” *Opt. Express*, vol. 20, no. 3, p. 2507, 2012, doi: 10.1364/oe.20.002507.

[10] D. Liang, G. Kurczveil, M. Fiorentino, S. Srinivasan, J. E. Bowers, and R. G. Beausoleil, “A tunable hybrid III-V-on-Si MOS microring resonator with negligible tuning power consumption,” in *2016 Optical Fiber Communications Conference and Exhibition, OFC 2016*, 2016, doi: 10.1364/ofc.2016.th1k.4.

[11] E. Li, B. A. Nia, B. Zhou, and A. X. Wang, “Transparent conductive oxide-gated silicon microring with extreme resonance wavelength tunability,” *Photonics Res.*, 2019, doi: 10.1364/prj.7.000473.

[12] S. Campione *et al.*, “Submicrometer Epsilon-Near-Zero Electroabsorption Modulators Enabled by High-Mobility Cadmium Oxide,” *IEEE Photonics J.*,

vol. 9, no. 4, 2017, doi: 10.1109/JPHOT.2017.2723299.

[13] R. Hashimoto, Y. Abe, and T. Nakada, “High mobility titanium-doped In2o3 thin films prepared by sputtering/post-annealing technique,” *Appl. Phys. Express*, vol. 1, no. 1, pp. 2–5, 2008, doi: 10.1143/APEX.1.015002.

[14] V. R. Almeida, R. R. Panepucci, and M. Lipson, “Nanotaper for compact mode conversion,” *Opt. Lett.*, vol. 28, no. 15, p. 1302, 2003, doi: 10.1364/ol.28.001302.

[15] B. Ben Bakir *et al.*, “Low-Loss (< 1 dB) and polarization-insensitive edge fiber couplers fabricated on 200-mm silicon-on-insulator wafers,” *IEEE Photonics Technol. Lett.*, vol. 22, no. 11, pp. 739–741, 2010, doi: 10.1109/LPT.2010.2044992.

[16] S. Nambiar, P. Sethi, and S. K. Selvaraja, “Grating-assisted fiber to chip coupling for SOI photonic circuits,” *Appl. Sci.*, vol. 8, no. 7, pp. 1–22, 2018, doi: 10.3390/app8071142.

[17] I. Demirtzioglou *et al.*, “Frequency comb generation in a silicon ring resonator modulator,” *Opt. Express*, vol. 26, no. 2, p. 790, 2018, doi: 10.1364/oe.26.000790.

[18] Z. Tu, D. Gao, M. Zhang, and D. Zhang, “High-sensitivity complex refractive index sensing based on Fano resonance in the subwavelength grating waveguide micro-ring resonator,” *Opt. Express*, vol. 25, no. 17, p. 20911, 2017, doi: 10.1364/oe.25.020911.

[19] Z. Wang, X. Xu, D. L. Fan, Y. Wang, and R. T. Chen, “Trapezoidal shape subwavelength grating waveguide based high quality factor micro-ring resonator,” *2016 Conf. Lasers Electro-Optics, CLEO 2016*, vol. 41, no. 14, pp. 3375–3378, 2016.

[20] V. Donzella, A. Sherwali, J. Flueckiger, S. M. Grist, S. T. Fard, and L. Chrostowski, “Design and fabrication of SOI micro-ring resonators based on sub-wavelength grating waveguides,” *Opt. Express*, vol. 23, no. 4, p. 4791, 2015, doi: 10.1364/oe.23.004791.

[21] P. Cheben, R. Halir, J. H. Schmid, H. A. Atwater, and D. R. Smith, “Subwavelength integrated photonics,” *Nature*, vol. 560, no. 7720, pp. 565–572, 2018, doi: 10.1038/s41586-018-0421-7.

[22] Z. Wang, X. Xu, D. Fan, Y. Wang, H. Subbaraman, and R. T. Chen, “Geometrical tuning art for entirely subwavelength grating waveguide based integrated photonics circuits,” *Sci. Rep.*, vol. 6, no. May, 2016, doi: 10.1038/srep24106.

[23] J. Steinhauser, S. Faÿ, N. Oliveira, E. Vallat-Sauvain, and C. Ballif, “Transition

between grain boundary and intragrain scattering transport mechanisms in boron-doped zinc oxide thin films," *Appl. Phys. Lett.*, vol. 90, no. 14, pp. 2005–2008, 2007, doi: 10.1063/1.2719158.

[24] Q. Gao, E. Li, and A. X. Wang, "Comparative analysis of transparent conductive oxide electro-absorption modulators [Invited]," *Opt. Mater. Express*, vol. 8, no. 9, p. 2850, 2018, doi: 10.1364/ome.8.002850.

[25] W. Bogaerts *et al.*, "Silicon microring resonators," *Laser Photonics Rev.*, vol. 6, no. 1, pp. 47–73, 2012, doi: 10.1002/lpor.201100017.

[26] E. Li, Q. Gao, R. T. Chen, and A. X. Wang, "Ultracompact Silicon-Conductive Oxide Nanocavity Modulator with 0.02 Lambda-Cubic Active Volume," *Nano Lett.*, vol. 18, no. 2, pp. 1075–1081, 2018, doi: 10.1021/acs.nanolett.7b04588.

[27] B. Meng, J. Booske, and R. Cooper, "Extended Cavity Perturbation Technique to Determine the Complex Permittivity of Dielectric Materials," *IEEE Trans. Microw. Theory Tech.*, vol. 43, no. 11, pp. 2633–2636, 1995, doi: 10.1109/22.473190.

[28] M. Landgren and B. Jönsson, "Determination of the optical properties of Si/SiO2 surfaces by means of ellipsometry, using different ambient media," *J. Phys. Chem.*, vol. 97, no. 8, pp. 1656–1660, 1993, doi: 10.1021/j100110a030.

[29] H. N. Lee, H. J. Kim, and Y. M. Yoon, "Thin-film barriers using transparent conducting oxides for organic light-emitting diodes," *J. Soc. Inf. Disp.*, vol. 17, no. 9, p. 739, 2009, doi: 10.1889/jsid17.9.739.

[30] S. Liu, K. Xu, Q. Song, Z. Cheng, and H. K. Tsang, "Design of Mid-Infrared Electro-Optic Modulators Based on Aluminum Nitride Waveguides," *J. Light. Technol.*, vol. 34, no. 16, pp. 3837–3842, 2016, doi: 10.1109/JLT.2016.2587319.

[31] G. Yuan, L. Gao, Y. Chen, X. Liu, J. Wang, and Z. Wang, "Improvement of optical sensing performances of a double-slot-waveguide- based ring resonator sensor on silicon-on-insulator platform," *Optik (Stuttg).*, vol. 125, no. 2, pp. 850–854, 2014, doi: 10.1016/j.ijleo.2013.07.088.

[32] F. Dell'Olio and V. M. Passaro, "Optical sensing by optimized silicon slot waveguides," *Opt. Express*, vol. 15, no. 8, p. 4977, 2007, doi: 10.1364/oe.15.004977.

[33] L. Zhou, K. Okamoto, and S. J. B. Yoo, "Athermalizing and trimming of slotted silicon microring resonators with UV-sensitive PMMA upper-cladding," *IEEE Photonics Technol. Lett.*, vol. 21, no. 17, pp. 1175–1177, 2009, doi: 10.1109/LPT.2009.2023522.

[34] A. Kargar and C.-Y. Chao, "Design and optimization of waveguide sensitivity

in slot microring sensors," *J. Opt. Soc. Am. A*, vol. 28, no. 4, p. 596, 2011, doi: 10.1364/josaa.28.000596.